Extension of Vicarious Cold Calibration to 85–92 GHz for Spaceborne Microwave Radiometers

Rachael A. Kroodsma, *Student Member, IEEE*, Darren S. McKague, *Member, IEEE*, and Christopher S. Ruf, *Fellow, IEEE*

***Abstract*—Vicarious cold calibration in the frequency range of 85–92 GHz is analyzed. Vicarious cold calibration cannot be applied at these frequencies as easily as at lower frequencies due to greater sensitivity to water vapor and hydrometeor scattering. The effects of that sensitivity are mitigated by selective filtering of the high-frequency brightness temperatures (TBs) to remove those data where large amounts of water vapor and/or hydrometeor scattering are present. Potential filtering algorithms are presented, and the performance of each with respect to vicarious cold calibration TB stability is characterized. A scattering-based precipitation filter that utilizes a combination of both the lower frequencies from 19 to 37 GHz and the frequencies from 85 to 92 GHz is shown to be the most effective and easily implemented filter. For horizontal polarization, the theoretical minimum TB at the higher frequencies occurs at an unphysically high sea surface temperature (SST), which makes the vicarious cold statistic more sensitive to the population of actual SST values as well as the higher amounts of water vapor associated with warm SSTs. The statistic is stabilized in this case by considering the difference between observed and simulated vicarious cold TBs. Intercalibration between two radiometers using the vicarious cold calibration double difference method at high frequencies is shown to be greatly improved when using the precipitation filter.**

***Index Terms*—Calibration, microwave radiometry.**

I. Introduction

CALIBRATION of spaceborne microwave radiometer channels is important to ensure that consistent measurements are made. In addition to onboard calibration, external observations can be used as references to determine calibration errors that lie outside the onboard calibration loop or errors in the onboard calibration references themselves. Vicarious cold calibration is one such method which uses a stable statistic of the Earth brightness temperature (TB) as an external reference [1]. It has been successfully demonstrated for radiometer channels between 6 and 37 GHz [2], [3] but not previously in the 85–92-GHz range. Other methods for external calibration of radiometers carrying a high-frequency channel have been developed. These include the following: 1) averaging over-ocean observations for a long period of time to find scan biases; 2) comparisons with other radiometers using colocated observations; and 3) deep space maneuvers. These methods have been performed on the Special Sensor Microwave/Imager (SSM/I) [4], the Tropical Rainfall Measuring Mission Microwave Imager (TMI) [5], [6], and the Advanced Microwave Scanning Radiometer on the Earth Observing System platform (AMSR-E) [7], [8]. Method 1 is a straightforward method to implement; however, it requires averages of the TBs over several months to minimize the sensitivity to geophysical effects and thus washes out time-dependent calibration errors. Method 2 can be an effective method, but it requires that crossover locations between two radiometers exist and that there is a sufficiently large population of colocated observations. Method 3 is a very useful method where the spacecraft is rolled or pitched over so that the radiometer views cold space, creating a very stable cold background against which to calibrate. One potential limitation of this method is that the radiometer will experience changes in its thermal environment during the cold space maneuver that can alter (sometimes appreciably) the physical temperature of calibration-related hardware, thereby potentially altering characteristics of the calibration errors being investigated. In addition, not every platform is able to undergo this maneuver, so this method cannot be relied upon for every spaceborne radiometer.

Vicarious cold calibration is a useful calibration tool since it can be applied to a shorter time period than method 1, does not require crossover locations between radiometers as method 2 does, and is not dependent on a spacecraft maneuver as method 3 is. It is therefore desirable to extend vicarious cold calibration to the frequencies from 85 to 92 GHz since several current spaceborne radiometers utilize these frequencies, e.g., TMI at 85.5 GHz and the Special Sensor Microwave Imager/Sounder at 91.655 GHz [9]. However, using vicarious cold calibration at 85–92 GHz introduces several challenges that are not present at the lower frequencies. The theory of the vicarious cold calibration algorithm is that there exists a sea surface temperature (SST) where the microwave radiometer TB is at a minimum for given frequency, polarization, and Earth incidence angle (EIA). However, if this minimum does not exist, it could become difficult to derive a stable cold statistic. This

Manuscript received July 15, 2012; revised January 18, 2013; accepted April 24, 2013. Date of publication June 26, 2013; date of current version August 30, 2013. This work was supported in part by the National Aeronautics and Space Administration under Grant NNX10AM12H.

R. A. Kroodsma is with the Department of Atmospheric, Oceanic and Space Sciences, University of Michigan, Ann Arbor, MI 48109 USA (e-mail: rakro@umich.edu).

D. S. McKague and C. S. Ruf are with the Space Physics Research Laboratory, Department of Atmospheric, Oceanic and Space Sciences, University of Michigan, Ann Arbor, MI 48109 USA (e-mail: dmckague@umich.edu; cruf@umich.edu).

Color versions of one or more of the figures in this paper are available online at http://ieeexplore.ieee.org.

Digital Object Identifier 10.1109/TGRS.2013.2267152

is the case for the horizontal polarization (H-pol) frequencies around 90 GHz. The theoretical SSTs at which the 90-GHz TB is at a minimum are approximately 314 K for H-pol and 293 K for vertical polarization (V-pol) at an EIA of 55°. The SSTs around this value for each polarization are those that contribute to the coldest observed TBs. Since SSTs rarely exceed 310 K [10], the coldest TBs will not come from the SSTs around the theoretical 90-GHz H-pol minimum. Instead, the vicarious cold calibration statistic will use the coldest 90-GHz H-pol observations possible, but this calibration point may not be as stable as that at lower frequencies since it will depend on natural SST variability and, for a given SST distribution, on selection of the data population.

Furthermore, even though the 90-GHz V-pol vicarious cold SST is within the physical maximum bound, it occurs near the tropics where there is a high concentration of water vapor. Vicarious cold calibration minimizes the impact of atmospheric water vapor; however, it does not completely eliminate it from the cold calibration TB. The water vapor distribution in the atmosphere varies on seasonal and regional scales, and this can affect the stability of the cold calibration TB. This slightly affects the lower frequencies from 6 to 37 GHz, most noticeably for those channels around the water vapor absorption line. However, since the higher frequencies around 90 GHz are more sensitive to water vapor, the cold calibration TB will also be more sensitive to water vapor distribution. Since the effect of water vapor is to increase the top of atmosphere TB, the coldest TBs will then be found in regions where there is the least amount of water vapor (i.e., closer to the poles), even though the SST may be colder than that at the theoretical minimum TB. Therefore, it may not be a concern that the 90-GHz H-pol cold calibration TB occurs at an unphysically high SST, since the warm SSTs are masked by high amounts of atmospheric water vapor. Both the water vapor and SST distributions need to be accounted for so that geophysical variability is not included in the vicarious calibration and mistaken as a calibration offset.

A final concern with calibrating the 90-GHz channel that needs to be addressed is the TB depression caused by hydrometeor scattering [11]–[14]. Over an ocean background, the presence of water vapor serves to increase the TB through absorption. However, a decrease in the upwelling TB can occur through scattering. At 90 GHz, the scattering cross section of ice and liquid water is greater than that at lower frequencies, which results in more scattering and a greater TB depression. Wu and Weinman [11] modeled the TB for an atmosphere containing various amounts of liquid, mixed phase, and ice hydrometeors to show that the TB at 85 GHz can be greatly depressed by scattering due to the presence of ice. In many cases, the TBs can be lower than the theoretical cold TB from the surface. Wilheit *et al.* [12] observed TBs as low as 140 K at 92-GHz V-pol that were associated with strong raining regions and attributed them to scattering by ice. This TB is much lower than the coldest TBs produced from the ocean surface (about 230 K at 90 V). If these cold TBs are included in the vicarious cold calibration, the derived cold calibration TB will not be associated with the cold surface TBs but instead with the highly variable ice content. This introduces further variability into the vicarious cold calibration statistic that needs to be removed.

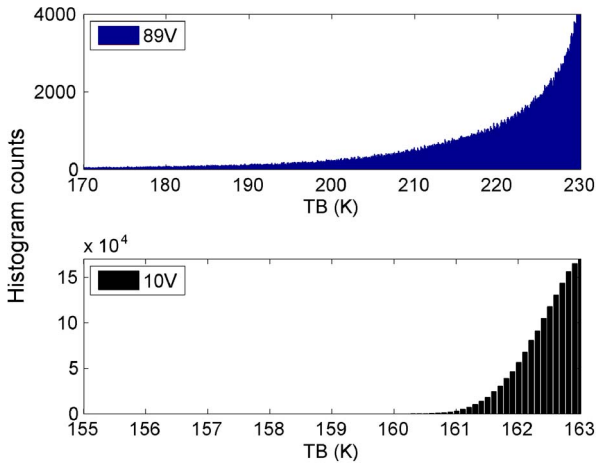

Fig. 1. Comparison of (top) AMSR-E 89V TB histogram with (bottom) the 10.7V TB histogram for January 2006. The long cold tail present for 89V is due to hydrometeor scattering, while 10.7V has a much sharper lower bound and a restricted cold tail primarily due to additive noise equivalent delta temperature noise. The long cold tail can destabilize the vicarious cold calibration statistic if not properly filtered.

This paper analyzes the stability of the 85–92-GHz vicarious cold calibration TB and assesses methods to address these challenges. The high-frequency 89-GHz channel on AMSR-E will be used as an example in this study, as will the TMI 85.5-GHz channel.

II. Vicarious Cold Calibration at 89 GHz

The concept of the vicarious cold calibration algorithm is that there exists a lower bound on the TB histogram from which a stable cold TB statistic can be derived. The TBs that make up the lower bound on the histograms are those due to cold ocean scenes with minimal atmospheric attenuation and calm winds. However, if the lower bound TBs are due to less stable conditions, e.g., hydrometeor scattering, it is difficult to derive a stable statistic since hydrometeor scattering is highly variable. This is the case for the high-frequency range of 85–92 GHz. Fig. 1 shows a sample histogram for AMSR-E 89-GHz V-pol (89V) (top) alongside 10.7-GHz V-pol (10.7V) (bottom). The TBs for both channels are from one month of data and are filtered for land, sea ice, and quality and binned into histograms using a TB resolution of 0.1 K. The 89V TB histogram has a long cold tail that is due to hydrometeor scattering as will be identified later. Deriving a cold calibration TB from this histogram would result in a cold calibration TB that is dependent on the highly variable hydrometeor scattering and not the stable ocean background. In contrast, the 10.7V TB histogram has a sharp lower bound. Under extreme conditions, hydrometeor scattering can occur at 10.7 GHz, but the TB depression is not large enough to cause TBs to be as cold as those generated from the surface. Therefore, the TBs that make up the lower bound of the 10.7V histogram are attributed to the ocean surface.

Fig. 2 shows the cold calibration TB over one year for AMSR-E 89V and 89-GHz H-pol (89H). The vicarious cold calibration algorithm is performed on one month of data for 12 months from July 2005 to June 2006. A description of how the vicarious cold calibration TB is derived is given in [1].

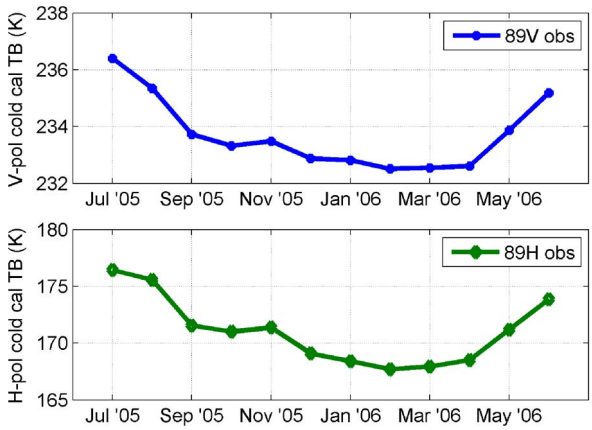

Fig. 2. Cold calibration TB for AMSR-E (top) 89V and (bottom) 89H. A seasonal cycle in the cold calibration TB is present for both polarizations but more strongly for H-pol. The ranges of variation over the year are approximately 4 K for V-pol and 9 K for H-pol.

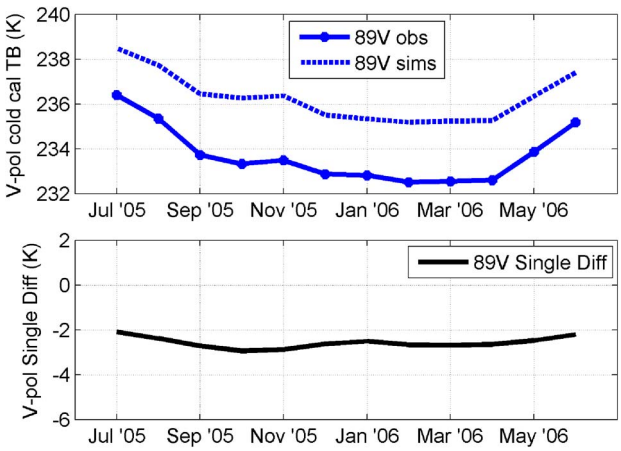

Fig. 3. Cold calibration TB for AMSR-E 89V (top) observed and simulated TBs and (bottom) SD by month for July 2005–June 2006.

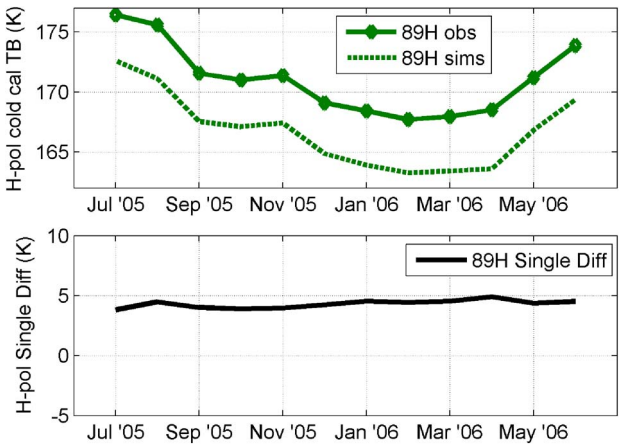

Fig. 4. Cold calibration TB for AMSR-E 89H (top) observed and simulated TBs and (bottom) SD by month for July 2005–June 2006. The simulations are able to model the seasonal variation in the cold calibration TB and reduce it in the SD.

The 89V channel has small variations in the cold calibration TB throughout the year, while the seasonal variation is very apparent in 89H. Note that the scales for V-pol and H-pol are different in order to show the seasonal variation for both polarizations. A possible reason for the greater seasonal variability in the H-pol cold calibration TB is that the relative TB contrast between the atmosphere and surface is greater for horizontally polarized TBs compared to vertically polarized TBs. Small changes in the atmospheric TB therefore have a greater effect on the overall top of atmosphere TB for H-pol, causing the cold calibration TB at H-pol to be more sensitive to atmospheric variability. Also, as noted before, the H-pol theoretical minimum TB is at a warmer SST than what occurs naturally, so the cold calibration TB at H-pol may be more dependent on SST variability, depending on the distribution of water vapor around the warm SSTs. This seasonal variation needs to be reduced, so it is not included in the calibration. One way to do this is by including simulated TBs in the calibration that account for geophysical variables such as water vapor and SST variations. By taking the difference between the cold calibration TB from the observations (obs) and the cold calibration TB derived from the simulations (sims), called the single difference (SD), the seasonal variation can be minimized. The radiative transfer model (RTM) used to simulate the TBs and the process of differencing the observed cold calibration TB from the simulated cold calibration TB is described in [3]. The extension of the simulations to include the high frequencies gives rise to the possibility of greater errors in the simulated TBs due to atmospheric water vapor and cloud liquid water (CLW) errors in the input fields to the RTM. However, since vicarious cold calibration only uses the coldest TBs in the histogram when deriving the cold calibration TB, these TBs only include minimal amounts of water vapor and CLW. Therefore, any errors in the simulated cold calibration TB due to water vapor and CLW will be small. Figs. 3 and 4 compare the observed cold calibration TB with the simulated cold calibration TB and illustrate the ability of the simulations to model the observations through the SD for both 89V and 89H. The reduction of the seasonal cycle is most evident in the 89H channel.

While the simulations do appear to improve the calibration by minimizing the seasonal signal, the simulations do not solve the problem of the long cold tail due to hydrometeor scattering. The RTM only accounts for absorption in the atmosphere and does not include any scattering. Further filtering of the TBs needs to be done to reduce the cold tail observed in the TB histogram in Fig. 1.

III. TB Filters

We hypothesize that the very cold TBs contributing to the long tail in the TB histograms are due to hydrometeor scattering. It is therefore necessary to find one or more filters that can remove data in which scattering occurs. It is not reasonable to simply remove any TBs below a given threshold in the histogram, since some of those cold TBs could be due to the surface signal.

One possible filter is to use the lower frequencies on the microwave radiometer to flag areas of precipitation. High rain rates tend to be correlated with areas of strong convection, which lead to formation of ice. Using the other channels of the radiometer to filter the high-frequency TBs allows filtering

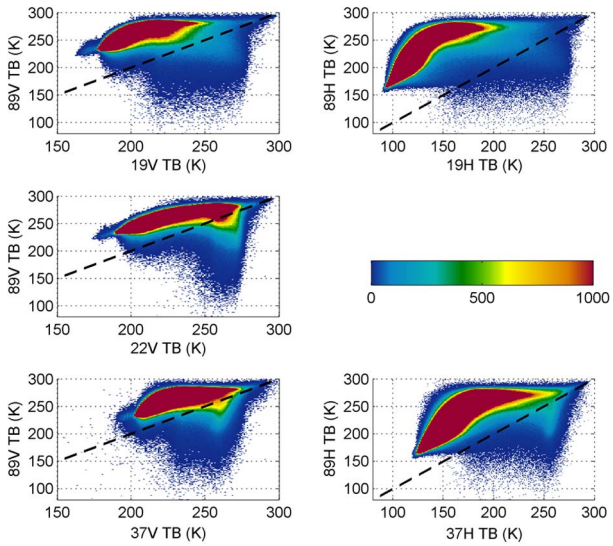

Fig. 5. Two-dimensional histograms of 89 GHz versus (top) 19 GHz, (middle) 22 GHz, and (bottom) 37 GHz. The left column shows V-pol, and the right shows H-pol. Colors indicate number of TB counts. Low 89-GHz TBs tend to be correlated with high TBs at the lower frequencies.

to be done without use of ancillary data. Stogryn *et al.* [15] developed four precipitation filters to apply to the SSM/I data that can be applied to AMSR-E as well. The data are flagged as precipitation if the following conditions occur:

$$\mathrm{TB}_{37\mathrm{V}} - \mathrm{TB}_{37\mathrm{H}} > 50\ \mathrm{K} \quad (1)$$

$$\mathrm{TB}_{19\mathrm{V}} > \mathrm{TB}_{37\mathrm{V}} \quad (2)$$

$$\mathrm{TB}_{19\mathrm{H}} > 185\ \mathrm{K} \quad (3)$$

$$\mathrm{TB}_{37\mathrm{H}} > 210\ \mathrm{K}. \quad (4)$$

In addition to these low-frequency flags, a set of high-/low-frequency combinations can be used to flag the data for precipitation [16], [17]. Filters were developed by examining 2-D histograms of the various combinations of 89 GHz versus 19, 22, and 37 GHz of similar polarizations. These plots are shown in Fig. 5 for one month of data. For both polarizations, it is apparent that there is a correlation between low TBs at 89 GHz with high TBs at 19, 22, and 37 GHz. This is expected since higher amounts of water vapor and precipitation will increase the TBs observed at the lower frequencies, while at the same time decreasing the TBs at 89 GHz through scattering. These plots can be used to develop filters for 89 GHz. The black dashed line in each plot in Fig. 5 is the 1:1 line where the TBs at each frequency are equal. For all frequency combinations, many of the very cold TBs at 89 GHz can be filtered from the data by removing TBs below the black dashed line. If there was no atmosphere on top of the ocean background, a higher frequency would result in a higher top-of-atmosphere TB due to the increase of surface emissivity with frequency. Therefore, all the TBs below the black dashed line should be from regions where there is a significant amount of atmospheric contribution which decreases the 89-GHz TB relative to the lower frequency channels, as would be expected from atmospheric scattering. This filter will be analyzed in the next section.

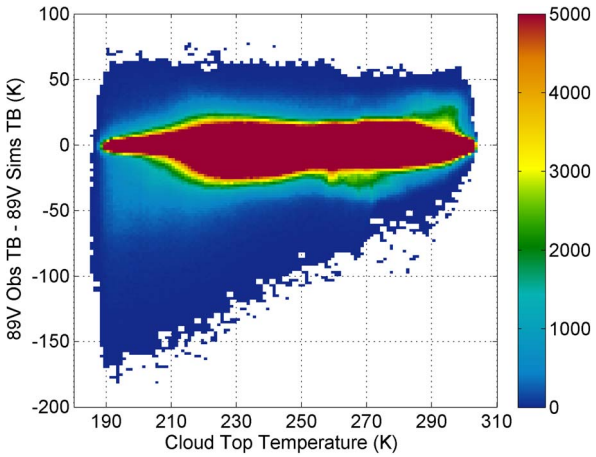

Fig. 6. Two-dimensional histogram of 89V observed TBs minus simulated TBs versus CTT for January 2006. Colors indicate number of counts. The magnitude of the scattering increases with decreasing CTT.

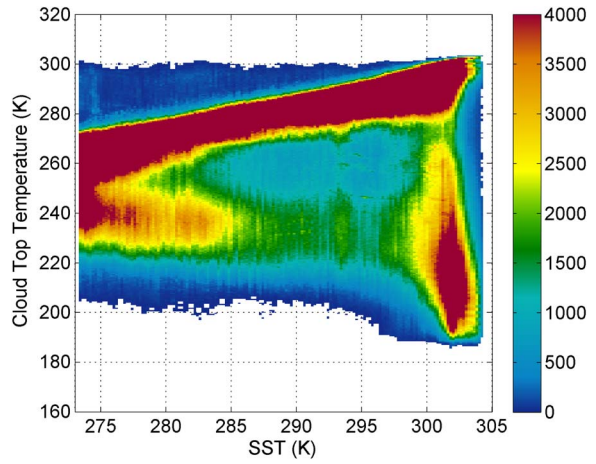

Fig. 7. CTT versus SST 2-D histogram for January 2006. Colors indicate number of counts. Most of the very cold CTTs occur at high SSTs.

One potentially useful filter that requires ancillary data is cloud top temperature (CTT). CTT products can be derived from infrared (IR) sensors. Cold CTTs are correlated with areas of strong convection, so knowledge of the CTTs could greatly help in reducing the hydrometeor scattering signature in the TB data. The Aqua platform which has AMSR-E on board conveniently also has a visible/IR imager, the Moderate Resolution Imaging Spectroradiometer (MODIS). MODIS Level 2 products contain a CTT field [18] that can be used to filter AMSR-E TB data. The MODIS swath is wide enough to cover the entire AMSR-E scan, with a small time difference of approximately 2 min separating the MODIS observations from the AMSR-E observations.

Fig. 6 shows a 2-D histogram of the difference between the AMSR-E observed TBs and simulated TBs versus the CTT for 89V. The CTT fields from MODIS are regridded to the AMSR-E observations using a linear interpolation. The plot has an asymmetrical shape, showing a large region of data at cold CTTs where the observed TB is less than the simulated TB. Since the simulations do not include the effect of scattering, the simulated TB will be warmer than the observed TB in regions

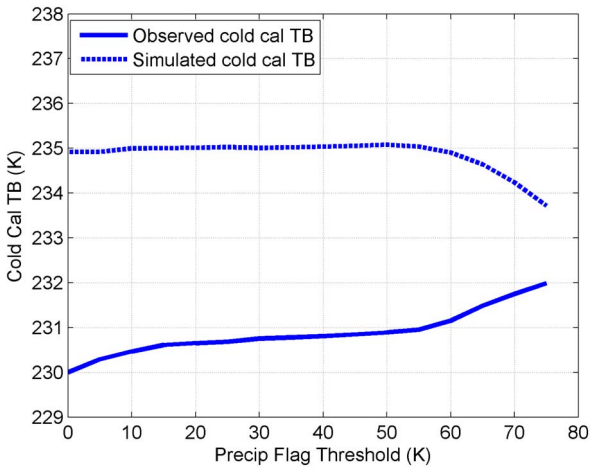

Fig. 8. Observed and simulated cold calibration TBs using different filter thresholds for 37V–37H.

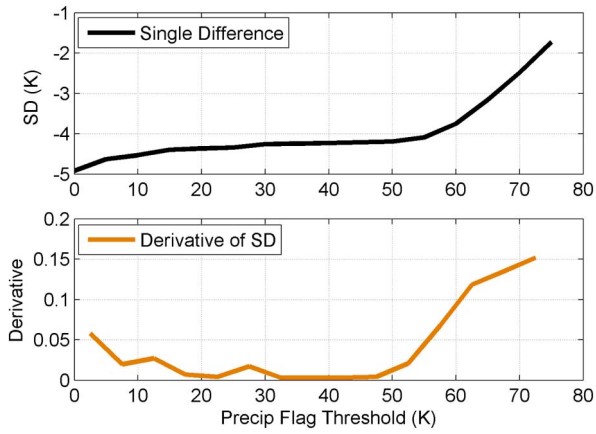

Fig. 9. SD and the derivative of the SD with respect to the TB threshold. A threshold of 50 K is a reasonable value for the filter.

of hydrometeor scattering. As seen in Fig. 6, the magnitude of the scattering increases with decreasing CTT.

Another useful application of the CTT fields is to find SSTs that are associated with cold CTTs, so that an SST filter can be applied to the data. Fig. 7 shows a 2-D histogram of CTT versus SST for one month of data (January 2006). The SST fields are taken from the Global Data Assimilation System (GDAS), which is used as input to the RTM. The SST where the theoretical minimum TB occurs for 89V ($\sim$293 K) has very few cold CTTs associated with it compared to SSTs colder and warmer than 293 K. H-pol presents a different challenge, since its theoretical minimum TB occurs at SSTs higher than what occurs naturally. Therefore, the coldest surface TBs at H-pol will occur at the warmest SSTs that exist with minimal amounts of water vapor. As seen in Fig. 7, the warmest SSTs are associated with cold CTTs and, therefore, a high probability of hydrometeor scattering. If the SSTs were restricted for H-pol, this might help eliminate much of this scatter effect on the vicarious cold calibration TBs.

IV. Application of TB Filters

The three types of potential filters to apply to the high-frequency TBs include a precipitation filter derived from combinations of low/high microwave frequencies, a CTT filter using MODIS data, and an SST filter using GDAS data. Each of these filters is analyzed to determine what threshold value is appropriate to stabilize the vicarious cold calibration TB.

The filter in (1) uses the difference between V-pol and H-pol at 37 GHz to look for the polarization signature from precipitation. The threshold in this equation is analyzed to determine whether 50 K is the appropriate value to use as a high-frequency TB filter. This threshold value is varied from 0 to 70 K, and the filter is applied to the 89-GHz observed and simulated TBs. The vicarious cold calibration algorithm is then performed on both the observed and simulated TBs, and the results are plotted in Fig. 8 for 89V. A sign that the filter is properly removing cold TBs due to scattering and not the surface signal is that the observed cold calibration TB is warming while the simulated cold calibration TB (which does not include scattering) remains unchanged. Fig. 9 shows this SD as well as the derivative of the SD with respect to the precipitation filter threshold. The objective of this analysis is to determine the optimal threshold value to remove scattering effects. As the threshold value is increased, more TBs are filtered out, which, in turn, affects the derived cold calibration TB. At some point, increasing the threshold further destabilizes the SD as the sample size becomes too small. This effect can be seen by looking at the derivative of the SD with respect to the threshold. In Fig. 9, this transition occurs around 50 K. Below 50 K, the SD is increasing steadily at a constant rate. This increase is due to the warming of the observed cold calibration TB while the simulated cold calibration TB remains unchanged, as shown in Fig. 8, since the filter is removing only those regions of high scattering. Above 50 K, the SD and its derivative increase rapidly with increasing threshold, indicating relative instability of the vicarious cold calibration statistic. We therefore use a precipitation flag threshold of 50 K, supporting the findings in [15]. The AMSR-E data used in this analysis are from July 2005 only; however, the other data follow the same general pattern.

The other filters that make use of the radiometer's lower frequencies are those combinations shown in Fig. 5. A similar analysis to the one for 37-GHz V-pol (37V)/37-GHz H-pol (37H) previously mentioned is performed for these five combinations to derive the filters given in

$$\mathrm{TB}_{89\mathrm{V}} > \mathrm{TB}_{19\mathrm{V}} + 10\ \mathrm{K} \tag{5}$$

$$\mathrm{TB}_{89\mathrm{H}} > \mathrm{TB}_{19\mathrm{H}} + 30\ \mathrm{K} \tag{6}$$

$$\mathrm{TB}_{89\mathrm{V}} > \mathrm{TB}_{22\mathrm{V}} \tag{7}$$

$$\mathrm{TB}_{89\mathrm{V}} > \mathrm{TB}_{37\mathrm{V}} \tag{8}$$

$$\mathrm{TB}_{89\mathrm{H}} > \mathrm{TB}_{37\mathrm{H}} + 10\ \mathrm{K}. \tag{9}$$

These five combinations as well the 37V/37H combination previously mentioned are collectively used as the precipitation filter.

The CTT and SST filters are also analyzed according to the method described previously. It is found that a filter which

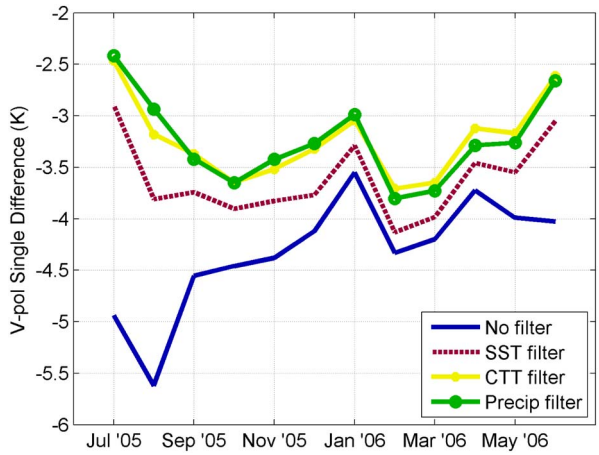

Fig. 10. SD for AMSR-E 89V with various filters applied. The precipitation filter and CTT filter give the best performance.

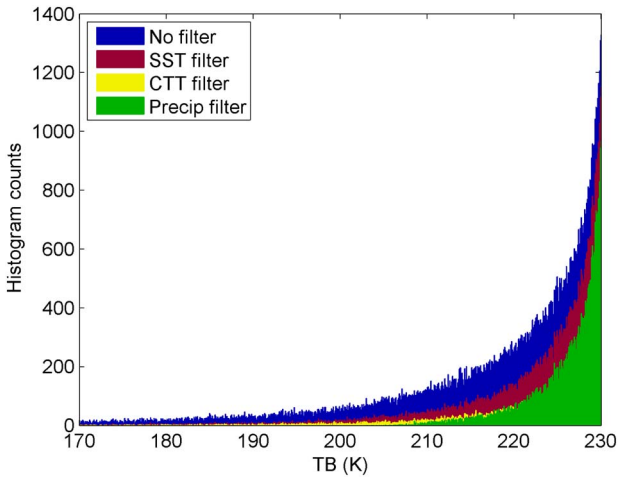

Fig. 11. TB histograms for 89V with various filters applied. The precipitation filter removes the largest percentage of the cold tail.

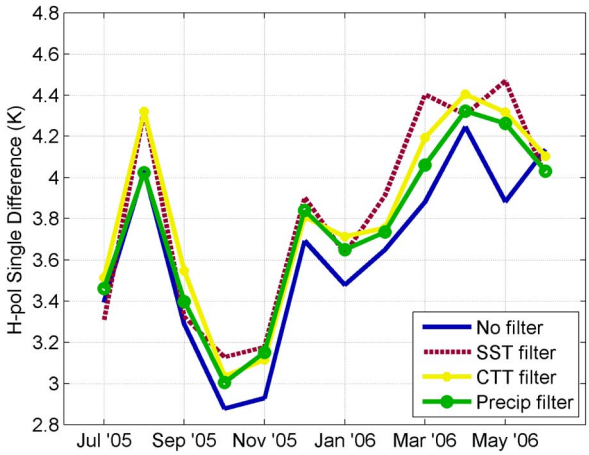

Fig. 12. SD for AMSR-E 89H with various filters applied. The filters do not have as significant an impact on the cold calibration TB for H-pol as they do for V-pol.

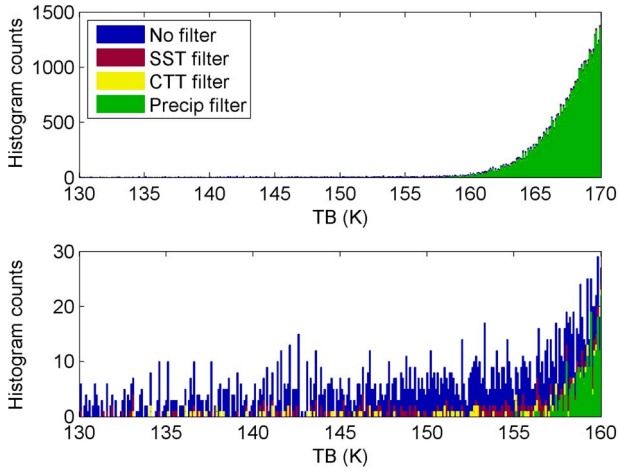

Fig. 13. TB histograms for 89H with different filters applied. The bottom plot has a smaller TB range to highlight the cold tail. H-pol does not have a significant cold tail, but the precipitation filter removes what little tail there is.

removes all pixels with CTT below 230 K is effective at eliminating hydrometeor scattering. The scattering is also effectively removed by a filter that removes regions where the SST is greater than 300 K for both polarizations. These three filters are applied to both the V-pol and H-pol 89-GHz TBs in the following analysis.

A. V-Pol

Fig. 10 shows the cold calibration TB SD for AMSR-E 89V using the various filters described previously. Each of the three filters improves the observed cold calibration TB; however, it does not appear necessary to use the SST filter, since the precipitation filter improves the cold calibration TB beyond that of the SST filter. Also, since the CTT filter and precipitation filter give approximately the same improvement to the cold calibration TB, it is not necessary to use both of them. It is far more convenient to use the precipitation filter rather than the CTT filter since it does not require colocated IR data.

Fig. 11 shows the cold end of the TB histograms after applying the various filters for one month of AMSR-E observations. The effect of each filter on removing the cold tail of the histogram can be seen. The SST filter removes part of the tail, while the CTT and precipitation filters remove more of the tail. This gives a lower bound to the TB histogram that is associated with the cold surface TBs and not hydrometeor scattering, leading to a derived cold calibration TB that has greater stability.

B. H-Pol

Fig. 12 shows the AMSR-E 89H cold calibration TB SD with the three filters applied. The filters make a less significant impact for H-pol than they do at V-pol. One reason for this could be that H-pol does not have as large of a cold tail in the histogram due to scattering. Since the H-pol cold calibration TB is much lower than V-pol (about 165 K at H-pol compared with 230 K at V-pol), there are not as many cold TBs from hydrometeor scattering that are colder than the H-pol cold calibration TB relative to the V-pol cold calibration TB. This can be seen in the TB histograms for H-pol shown in Fig. 13. While there is a slight cold tail in the histogram, it is not nearly as substantial as the tail at V-pol (see Fig. 11). The bottom plot

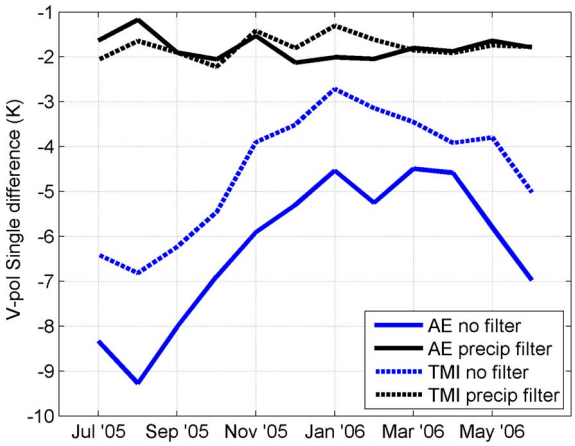

Fig. 14. SDs for AMSR-E and TMI V-pol comparing no filter and the precipitation filter. The filtering has a significant positive impact on the SD.

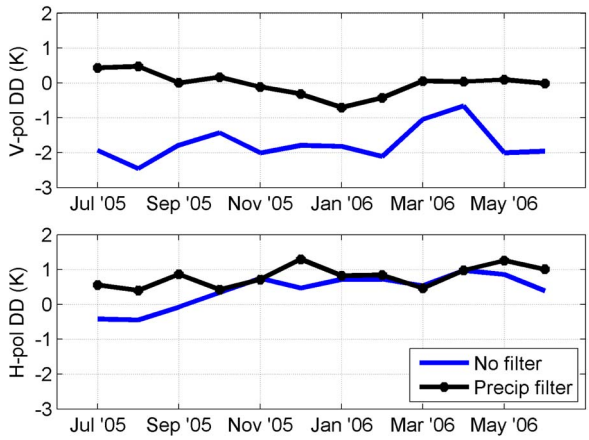

Fig. 15. DD for AMSR-E–TMI (top) V-pol and (bottom) H-pol. With the precipitation filter, the DDs are −0.03 K for V-pol and 0.80 K for H-pol, while with no filter, they are −1.75 K for V-pol and 0.40 K for H-pol (averaged over the 12 months).

in Fig. 13 shows the same histogram as the top, with a smaller TB range to better observe the cold tail. What little tail does exist in the H-pol TB histogram is removed by the precipitation filter.

The other concern with H-pol aside from hydrometeor scattering is the unphysical SST at which the theoretical cold TB occurs. The SST filter was implemented with the hope that it would be able to limit the regions where the H-pol cold calibration TB is derived to stabilize the statistic. However, the SST filter does not appear to improve the calibration any more than the other filters. This is most likely due to the vicarious cold calibration TB not being sensitive to the warm SSTs since the algorithm naturally filters out regions of high water vapor, and these regions most often occur at the warmest SSTs. Unlike in V-pol, not one filter appears to perform better than any of the other filters. Since the precipitation filter is the best for V-pol and is shown to be the filter that best removes the H-pol histogram cold tail, as seen in Fig. 13, this will be the filter implemented for the H-pol TBs.

V. Intercalibration of AMSR-E With TMI

Intercalibration using the vicarious cold calibration double difference (DD) method has been shown to be an effective method for frequencies from 10 to 37 GHz [3]. It is important to be able to intercalibrate the high-frequency channels from 85 to 92 GHz as well.

The precipitation filter was shown to be the most effective and convenient filter to use, so this will be applied here to intercalibrate the AMSR-E 89-GHz channel with the TMI 85.5-GHz channel. Based on analysis of TMI data sensitivity to precipitation flag thresholds, the same TB thresholds for the AMSR-E precipitation filter as given in (1) and (5)–(9) are used for TMI. It becomes even more evident that the cold TBs from hydrometeor scattering need to be filtered when performing intercalibration. Fig. 14 shows the SD for both AMSR-E and TMI using no filter compared with using the precipitation filter. AMSR-E latitudes have been limited to -40° to $+40^\circ$ so that the latitude sampling is similar to TMI. This large difference in the SD between no filter and the precipitation filter is due to the difference in the observed cold calibration TB, since the precipitation filter has an insignificant effect on the simulated cold calibration TB. Fig. 15 shows the DD for V-pol (top) and H-pol (bottom) AMSR-E–TMI. The precipitation filter has a large impact on the V-pol DD value. The value of the V-pol DD when averaging over the 12 months is −0.03 K with the precipitation filter, compared to −1.75 K without the filter. If the hydrometeor scattering is not properly accounted for, it could be taken as a calibration offset when, in fact, it is geophysical in origin. The precipitation filter does not have as great an effect on the DD for H-pol as it does for V-pol, as seen previously for the AMSR-E SD. The values of the H-pol DD when taking the average over the year are 0.80 K with the precipitation filter and 0.40 K without the filter. The objective of the DD is not to achieve a value as close to zero as possible but to have confidence that the DD contains as few geophysical effects as possible, leaving just a calibration difference between the two radiometers. Even though the H-pol DD without the precipitation filter is closer to zero than that with the filter, it is not as accurate, so the DD with the filter is preferred.

TABLE I
SDs and DDs for AMSR-E and TMI Intercalibration, Averaged Over July 2005 to June 2006. The Effect of the Precipitation Filter Is More Pronounced for V-pol

	V-pol		H-pol	
	No filter	**Precip filter**	**No filter**	**Precip filter**
AMSR-E Single Difference (K)	-6.28	-1.80	4.04	4.75
TMI Single Difference (K)	-4.53	-1.77	3.64	3.95
Double Difference (K)	-1.75	-0.03	0.40	0.80

Table I summarizes the results from Figs. 14 and 15. The values given are the averages of the SDs and DDs over a year. It is difficult to assess the absolute accuracy of the vicarious cold calibration method, since that would require identifying a radiometer or model as truth. Potential inaccuracies in the forward model, such as errors in the surface dielectric or atmospheric absorption model, are important to consider if absolute

calibration is desired. However, we are only concerned here with the relative stability of the vicarious cold calibration, so that this method can be used to identify a calibration difference between two radiometers or the stability of a radiometer's calibration through the SD. A potential contributor to instability in the cold calibration is seasonal variability, which will manifest itself in the SD if it is not properly accounted for. This relative stability can be quantified using the standard deviation of the SD over a year of data. The standard deviations of the AMSR-E precipitation filtered data are 0.27 K for V-pol and 0.34 K for H-pol. Compared to the prefiltered data, which have standard deviations of 1.61 K for V-pol and 0.59 K for H-pol, the filtered data improve the relative stability.

VI. Conclusion

Vicarious cold calibration in the frequency range of 85–92 GHz has been analyzed and shown to be a useful calibration tool if the TBs are properly filtered. The challenges associated with vicarious cold calibration at these frequencies include contamination of the cold TBs due to hydrometeor scattering, a higher sensitivity to atmospheric water vapor, and the theoretical H-pol cold calibration TB occurring at an unphysical SST. Various filters were applied to the high-frequency TBs, and each filter was analyzed to determine its performance on the vicarious cold calibration TB. The filters applied included a precipitation filter derived from low-frequency TBs, a CTT filter using ancillary data, and an SST filter. The precipitation and CTT filters were found to be the most effective at removing the cold TB contamination due to scattering for V-pol. The 89H channel was found to be less affected by the filters than V-pol was. However, it was shown to be the more sensitive of the two polarizations to seasonal geophysical variability. This sensitivity was minimized by using modeled TBs to derive a simulated cold calibration TB to match the observed cold calibration TB. The effect of using the precipitation filter was shown through intercalibration of the V-pol channel, where the precipitation filter improved the average cold calibration difference between AMSR-E and TMI by 1.7 K. Beyond intercalibration of radiometers, this calibration tool can also be used for identifying radiometer drifts as well as anomalies across the scan for scanning radiometers. For these analyses, it is also important to filter for hydrometeor scattering, since it could mistakenly be classified as a drift in the radiometer or TB scan bias.

References

[1] C. S. Ruf, "Detection of calibration drifts in spaceborne microwave radiometers using a vicarious cold reference," *IEEE Trans. Geosci. Remote Sens.*, vol. 38, no. 1, pp. 44–52, Jan. 2000.

[2] D. S. McKague, C. S. Ruf, and J. J. Puckett, "Beam spoiling correction for spaceborne microwave radiometers using the two-point vicarious calibration method," *IEEE Trans. Geosci. Remote Sens.*, vol. 49, no. 1, pp. 21–27, Jan. 2011.

[3] R. A. Kroodsma, D. S. McKague, and C. S. Ruf, "Inter-calibration of microwave radiometers using the vicarious cold calibration double difference method," *IEEE J. Sel. Topics Appl. Earth Observ. and Remote Sens.*, vol. 5, no. 3, pp. 1006–1013, Jun. 2012.

[4] J. P. Hollinger, J. L. Peirce, and G. A. Poe, "SSM/I instrument evaluation," *IEEE Trans. Geosci. Remote Sens.*, vol. 28, no. 5, pp. 781–790, Sep. 1990.

[5] C. Kummerow, W. Barnes, T. Kozu, J. Shiue, and J. Simpson, "The Tropical Rainfall Measuring Mission (TRMM) sensor package," *J. Atmos. Ocean. Technol.*, vol. 15, no. 3, pp. 809–817, Jun. 1998.

[6] F. J. Wentz, P. Ashcroft, and C. Gentemann, "Post-launch calibration of the TRMM Microwave Imager," *IEEE Trans. Geosci. Remote Sens.*, vol. 39, no. 2, pp. 415–422, Feb. 2001.

[7] T. Kawanishi, T. Sezai, Y. Ito, K. Imaoka, T. Takeshima, Y. Ishido, A. Shibata, M. Miura, H. Inahata, and R. W. Spencer, "The Advanced Microwave Scanning Radiometer for the Earth Observing System (AMSR-E), NASDA's contribution to the EOS for global energy and water cycle studies," *IEEE Trans. Geosci. Remote Sens.*, vol. 41, no. 2, pp. 184–194, Feb. 2003.

[8] K. Imaoka, Y. Fujimoto, M. Kachi, T. Takeshima, K. Shiomi, H. Mikai, T. Mutoh, M. Yoshikawa, and A. Shibata, "Post-launch calibration and data evaluation of AMSR-E," in *Proc. IEEE IGARSS*, Jul. 2003, vol. 1, pp. 666–668.

[9] D. B. Kunkee, G. A. Poe, D. J. Boucher, S. D. Swadley, Y. Hong, J. E. Wessel, and E. A. Uliana, "Design and evaluation of the first Special Sensor Microwave Imager/Sounder," *IEEE Trans. Geosci. Remote Sens.*, vol. 46, no. 4, pp. 863–883, Apr. 2008.

[10] R. W. Reynolds and T. M. Smith, "A high-resolution global sea surface temperature climatology," *J. Climate*, vol. 8, no. 6, pp. 1571–1583, Jun. 1995.

[11] R. Wu and J. A. Weinman, "Microwave radiances from precipitating clouds containing aspherical ice, combined phase, and liquid hydrometeors," *J. Geophys. Res.*, vol. 89, no. D5, pp. 7170–7178, Aug. 1984.

[12] T. T. Wilheit, A. T. C. Chang, J. L. King, E. B. Rodgers, R. A. Nieman, B. M. Krupp, A. S. Milman, J. S. Stratigos, and H. Siddalingaiah, "Microwave radiometric observations near 19.35, 92, and 183 GHz of precipitation in tropical storm Cora," *J. Appl. Meteorol.*, vol. 21, no. 8, pp. 1137–1145, Aug. 1982.

[13] I. M. Hakkarinen and R. F. Adler, "Observations of convective precipitating at 92 and 183 GHz: Aircraft results," *Meteorol. Atmos. Phys.*, vol. 38, no. 3, pp. 164–182, 1988.

[14] R. W. Spencer, H. M. Goodman, and R. E. Hood, "Precipitation retrieval over land and ocean with the SSM/I: Identification and characteristics of the scattering signal," *J. Atmos. Oceanic. Technol.*, vol. 6, no. 2, pp. 254–273, Apr. 1989.

[15] A. P. Stogryn, C. T. Butler, and T. J. Bartolac, "Ocean surface wind retrievals from Special Sensor Microwave/Imager data with neural networks," *J. Geophys. Res.*, vol. 90, no. C1, pp. 981–984, Jan. 1994.

[16] N. C. Grody, "Classification of snow cover and precipitation using the Special Sensor Microwave Imager," *J. Geophys. Res.*, vol. 96, no. D4, pp. 7423–7435, Apr. 1991.

[17] R. F. Adler, A. J. Negri, P. R. Keehn, and I. M. Hakkarinen, "Estimation of monthly rainfall over Japan and surrounding waters from a combination of low-orbit microwave and geosynchronous IR data," *J. Appl. Meteorol.*, vol. 32, no. 2, pp. 335–356, Feb. 1993.

[18] S. Platnick, M. D. King, S. A. Ackerman, W. P. Menzel, B. A. Baum, J. C. Riedi, and R. A. Frey, "The MODIS cloud products: Algorithms and examples from Terra," *IEEE Trans. Geosci. Remote Sens.*, vol. 41, no. 2, pp. 459–473, Feb. 2003.

Rachael A. Kroodsma (S'09) received the B.S.E. degree in earth systems science and engineering and the M.S.E. degree in electrical engineering from the University of Michigan, Ann Arbor, MI, USA, in 2009 and 2013, respectively, where she is currently working toward the Ph.D. degree in atmospheric and space science.

Her research interests include development of calibration techniques for microwave radiometers, with an emphasis on intercalibration of the radiometers for the Global Precipitation Measurement mission.

Darren S. McKague (M'08) received the Ph.D. degree in astrophysical, planetary, and atmospheric sciences from the University of Colorado, Boulder, CO, USA, in 2001.

He is currently an Assistant Research Scientist with the Department of Atmospheric, Oceanic and Space Sciences, University of Michigan, Ann Arbor, MI, USA, where he is also the Assistant Director of the Space Physics Research Laboratory. Prior to working with the University of Michigan, he was a Systems Engineer with Ball Aerospace and with Raytheon and was a Research Scientist with Colorado State University, Fort Collins, CO. His work has focused on remote sensing with emphases on the development of spaceborne microwave remote sensing hardware, passive microwave calibration techniques, and mathematical inversion techniques for geophysical retrievals. His experience with remote sensing hardware includes systems engineering for several advanced passive and active instrument concepts and the design of the calibration subsystem on the Global Precipitation Mission (GPM) Microwave Imager and the development of calibration techniques for the GPM constellation while with the University of Michigan. His algorithm experience includes the development of a near-real-time algorithm for the joint retrieval of water vapor profiles, temperature profiles, cloud liquid water path, and surface emissivity for the Advanced Microwave Sounding Unit at Colorado State University and the development of the precipitation rate, precipitation type, sea ice, and sea surface wind direction algorithms for the risk reduction phase of the Conical scanning Microwave Imager/Sounder.

Christopher S. Ruf (S'85–M'87–SM'92–F'01) received the B.A. degree in physics from Reed College, Portland, OR, USA, and the Ph.D. degree in electrical and computer engineering from the University of Massachusetts, Amherst, MA, USA.

He was with Intel Corporation, Hughes Space and Communication, the National Aeronautics and Space Administration (NASA) Jet Propulsion Laboratory, Pasadena, CA, USA, and Pennsylvania State University, University Park, PA, USA. In 2000, he was a Guest Professor with the Technical University of Denmark, Lyngby, Denmark. He is currently a Professor of atmospheric, oceanic, and space sciences and of electrical engineering and computer science with the Department of Atmospheric, Oceanic and Space Sciences, University of Michigan, Ann Arbor, MI, USA, where he is also the Director of the Space Physics Research Laboratory. He is also the Principal Investigator of the NASA EV-2 Cyclone Global Navigation Satellite System mission. He has served on the editorial boards of American Geophysical Union (AGU) *Radio Science* and American Meteorological Society (AMS) *Journal of Atmospheric and Oceanic Technology*. His research interests include GNSS-R bistatic scatterometry, microwave radiometry, sensor and technology development, and atmosphere and ocean geophysical retrieval algorithm development.

Dr. Ruf is a member of AGU, AMS, and Commission F of the Union Radio Scientifique Internationale. He has served on the editorial board of the IEEE TRANSACTIONS ON GEOSCIENCE AND REMOTE SENSING (TGRS). He was a recipient of four NASA Certificates of Recognition and seven NASA Group Achievement Awards, as well as the 1997 TGRS Best Paper Award, the 1999 IEEE Resnik Technical Field Award, and the 2006 IGARSS Best Paper Award.